Delft University of Technology

Document Version
Final published version

Licence
CC BY

Citation (APA)
Battal, F., Gupta, N., Mulder, P., Maasen, J., Poelma, R. H., Vlieg, E., & Schermer, J. J. (2026). Controlled Nano-Dendritic Structuring of Porous Copper Films via Pulse Electrochemical Deposition and Additive Chemistry. *Electrochemical Society. Journal*, *173*(6). https://doi.org/10.1149/ 1945-7111/ae51c6

Important note
To cite this publication, please use the final published version (if applicable).
Please check the document version above.

Copyright
In case the licence states "Dutch Copyright Act (Article 25fa)", this publication was made available Green Open Access via the TU Delft Institutional Repository pursuant to Dutch Copyright Act (Article 25fa, the Taverne amendment). This provision does not affect copyright ownership.
Unless copyright is transferred by contract or statute, it remains with the copyright holder.

Sharing and reuse
Other than for strictly personal use, it is not permitted to download, forward or distribute the text or part of it, without the consent of the author(s) and/or copyright holder(s), unless the work is under an open content license such as Creative Commons.

Takedown policy
Please contact us and provide details if you believe this document breaches copyrights.
We will remove access to the work immediately and investigate your claim.

This work is downloaded from Delft University of Technology.

Journal of The
Electrochemical Society

OPEN ACCESS

Controlled Nano-Dendritic Structuring of Porous Copper Films via Pulse Electrochemical Deposition and Additive Chemistry

To cite this article: Fatin Battal *et al* 2026 *J. Electrochem. Soc.* **173** 062502

View the article online for updates and enhancements.

You may also like

- 3-D Network Pore Structures in Copper Foams by Electrodeposition and Hydrogen Bubble Templating Mechanism
Wenbin Zhang, Chuang Ding, Aijun Wang et al.

- Effect of Bubble Behavior on the Morphology of Foamed Porous Copper Prepared via Electrodeposition
Hebing Zhang, Yinghua Ye, Ruiqi Shen et al.

- Three-Dimensional Porous Copper Structure with Corrosion Inhibitor Embedded for Active Corrosion Protection
Kaiyue Zhang, Lida Wang, Chuang Luo et al.

The New PAT-Cell-Solid!

EL-CELL®
electrochemical test equipment

Cycle Solid-State Batteries Under Controlled Pressure of up to 300 MPa (6 mm Diameter)!

Adjust and measure a force of up to 9000 N on the cell stack!
Force adjustment possible throughout the entire experiment

Built-in force, and temperature sensors!
With optional gas pressure sensor and gas in- and outlet

PAT-Solid-Core for easy assembly and reproducible results!
Press and cycle solid-state batteries with 6 or 10 mm electrode diameter

Cableless and highly sealed battery test cell!
For precise long-term measurements of solid-state cell chemistries

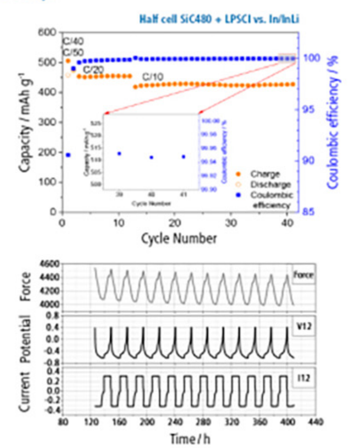

Learn more on our product website:

Download the data sheet (PDF):

Or contact us directly:
+49 40 79012-734
sales@el-cell.com
www.el-cell.com

This content was downloaded from IP address 154.59.124.113 on 26/03/2026 at 12:37

Journal of The Electrochemical Society, 2026 **173** 062502

Controlled Nano-Dendritic Structuring of Porous Copper Films via Pulse Electrochemical Deposition and Additive Chemistry

Fatin Battal,[1,z] Nikhil Gupta,[2] Peter Mulder,[1] Jeroen Maasen,[1] René H. Poelma,[2,3] Elias Vlieg,[1] and John J. Schermer[1]

[1] *Institute for Molecules and Materials, Radboud University, 6525AJ Nijmegen, The Netherlands*
[2] *Electronics Components Technology and Materials, Delft University of Technology, 2628CD Delft, The Netherlands*
[3] *Package Research and Development, Nexperia BV, 6534AB Nijmegen, The Netherlands*

Porous copper films with nanoscale dendritic architectures are of growing interest in various advanced technology domains. These copper films form a three-dimensional porous network with internal surfaces that are covered with "Romanesco-like" dendritic features. This study investigates the influence of pulse-assisted electrodeposition and targeted additive chemistry on the dynamic hydrogen bubble templating process and the resulting film morphology. It is found that duty cycle modulation controls pore size and distribution. SEM analysis reveals that deposition with 25% duty cycle produces films with nearly 50% smaller pores and significantly thinner, shorter dendritic branches compared to continuous deposition. The addition of chloride ions induces a transition from multi-branched dendrites to elongated fractal structures, whereas citric acid promotes smaller, more uniformly distributed pores by modifying hydrogen bubble dynamics. When both additives are present, each retains its dominant influence, with chloride shaping branch structure and citric acid refining macro porosity, together producing a well-balanced porous network. The ability to selectively control both pore size and dendritic/fractal nanostructures provides a versatile pathway to engineer porous copper films with tailored architectures to achieve application-specific properties through a scalable electrodeposition process.
© 2026 The Author(s). Published on behalf of The Electrochemical Society by IOP Publishing Limited. This is an open access article distributed under the terms of the Creative Commons Attribution 4.0 License (CC BY, https://creativecommons.org/licenses/by/4.0/), which permits unrestricted reuse of the work in any medium, provided the original work is properly cited. [DOI: 10.1149/1945-7111/ae51c6]

Manuscript submitted January 14, 2026; revised manuscript received March 4, 2026. Published March 24, 2026.

Supplementary material for this article is available online

Porous metallic materials represent a unique class of engineered structures that combine the inherent properties of metals (e.g., high electrical and thermal conductivity) with structural characteristics of foams (e.g., low density and large surface area).[1] Integration of porosity into metallic systems enables tunable physical behavior that makes these materials attractive in a broad spectrum of applications. The functional performance of porous metals is governed not only by the intrinsic properties of the metal itself but also the topology and morphology of the porous network including pore distribution, wall connectivity and ligament structure.[2] These features can be engineered across nano to macro scales to tailor transport phenomena such as mass diffusion, fluid flow, or electron/phonon conductivity.[3] As a result, porous metals are increasingly used in advanced technologies such as electrocatalysis, thermal interface materials, and, more recently, in electronics packaging applications.[4–7]

One of the most accessible and scalable methods for producing porous metallic films is through the Dynamic Hydrogen Bubble Templating (DHBT) method, where high cathodic current densities during electrodeposition induce simultaneous metal ion reduction and hydrogen gas evolution.[8,9] As schematically depicted in Fig. 1, DHBT relies on the formation, growth and detachment of hydrogen gas bubbles at the cathode surface, which act as dynamic in situ physical masks that locally obstruct metal deposition. At high cathodic currents used in DHBT, the deposition process enters a mass-transport-limited regime, where the local depletion of metal ions cannot be replenished quickly enough.[10] This imbalance promotes the growth of characteristic dendritic structures that feature multi-level branching (i.e., trunks, secondary and tertiary branches), as metal preferentially deposits at protrusions where ion flux is highest.[11] Simultaneously, hydrogen evolution shapes micron-scale pores by forcing these structures to grow around transient gas bubbles, yielding an interconnected porous network with a large surface area. The resulting films demonstrate a tortuous network composed of pores ranging from sub-micron to tens of microns and dendritic ligament walls. In the case of porous copper (Cu), the resulting films often display a "(nano-)dendritic" morphology in many cases resembling a "Romanesco-like" appearance that make up a macro-scale porous framework (Fig. 1d). These films are referred to as "porous copper" as well as "nano-dendritic copper" depending on the focus of the research or feature that is leading to an intended application.

Among various porous metals, porous copper (Cu) is of interest due to its good electrical and thermal properties, compatibility with a range of other metals (e.g., Sn, In, Ni, Ag), and its already established use in electronic systems.[12,13] In the broader context, "electronics packaging" encompasses the steps required to integrate a fabricated semiconductor die into a mechanically stable, electrically connected and thermally managed component.[14] In such a package, porous Cu films can also function as compliant layers that buffer thermal and mechanical stresses arising from local topographical variations or mismatches in thermal expansion. Accordingly, porous Cu films have been employed in various electronics packaging applications such as thermal interfaces, power electronics heat sink integration, ultra-fast sintering for die-attachment, hybrid interconnect systems and organics-free bonding interfaces.[4,6,12,13,15–17] Despite these demonstrated applications, a fundamental challenge of tunability remains, as the functional performance of porous Cu films is governed by their structural features, from pore size and distribution to branch length and connectivity. Thermal transport, mechanical integrity, and sintering behavior are all highly sensitive to these morphological parameters, yet most existing approaches yield structures with limited opportunity for systematic control. Without this ability to systematically tune both macro-scale porosity and nano-scale branch geometry, it is difficult to optimize porous Cu films for diverse applications. Thus, establishing such tunability is not only scientifically necessary to understand the coupled electrochemical growth mechanisms, but also technologically impactful as it enables tailoring of Cu films for various needs in packaging processes; from diffusion-driven bonding requiring finer porosity, to thermal interfaces requiring thicker walls. Consequently, the development of scalable fabrication strategies that provide pathways for structural tunability represents an essential step toward utilizing the full potential of porous Cu in electronics packaging and related technologies.

In this study, we present an approach for tailoring the morphology of nano-dendritic copper films through pulse-assisted

[z] E-mail: fatin.battal@ru.nl

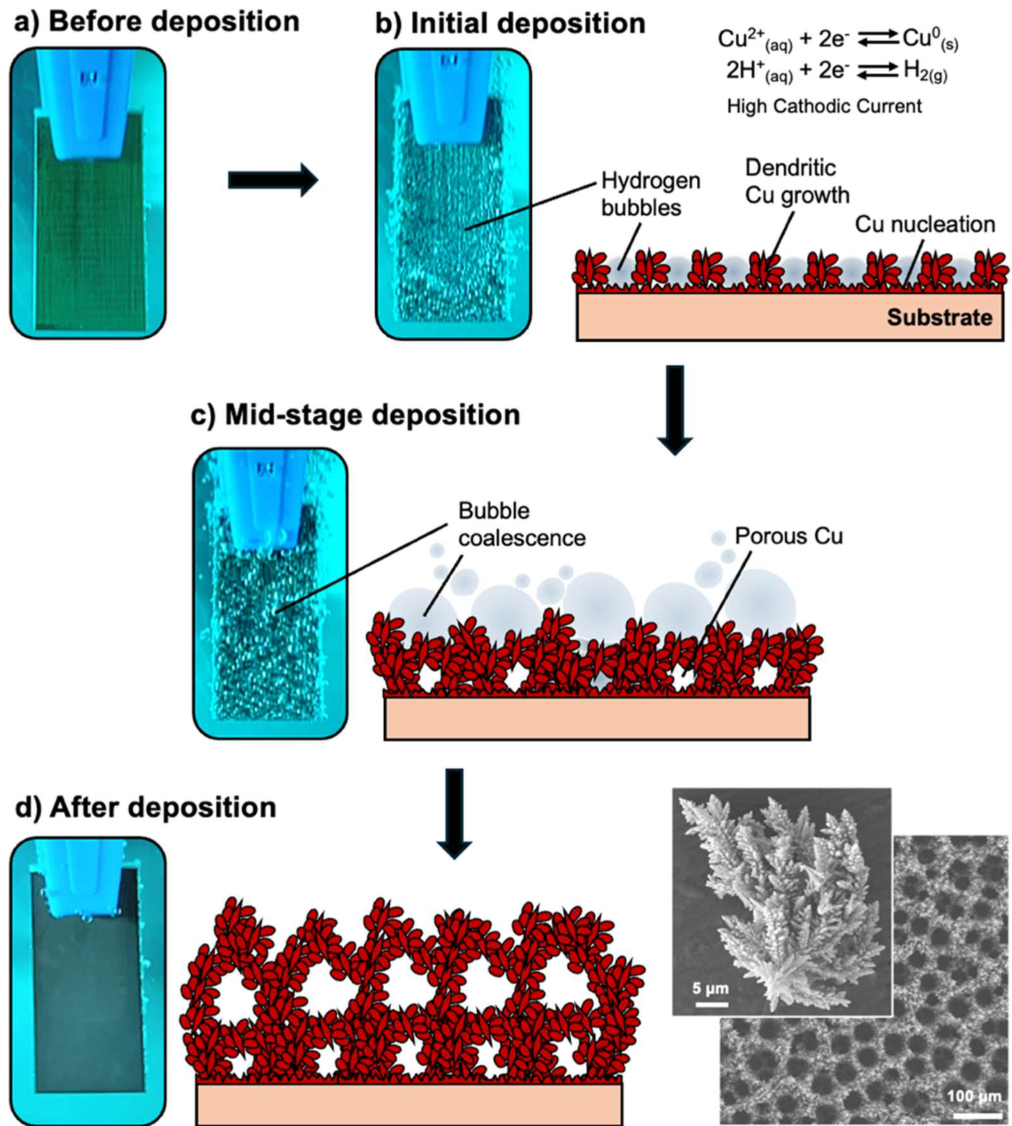

Figure 1. Schematic diagram of nano-dendritic copper deposition process through the DHBT method, high speed camera images of the sample during the different stages of the deposition process and SEM images of the final result. (a) Start of the process, initial copper growth followed by formation of initial dendrites and small hydrogen bubbles. (b) Dendritic growth continues, and pores become larger due hydrogen bubbles coalescence. (c) Formation of the final nano-dendritic porous network. (d) Top-view SEM image of a porous copper film manufactured via DHBT (lower image) and a stand-alone cluster of nano-dendritic copper structure (upper image).

electrochemical deposition (in short to be referred to as pulse deposition) based on the DHBT method, combined with targeted additive chemistry. The study first addresses the influence of the current density and duty cycle of the pulse deposition process on the resulting Cu films. Subsequently, the effect of additives to the electrolyte system is explored using common Cu deposition additives (e.g., SPS, JGB) as well as chloride ions and citric acid. The resulting films were then characterized using scanning electron microscopy (SEM) combined with image analysis to quantify the observed morphological features.

Experimental

Materials.— *Substrate preparation.*—All experiments were performed on substrates consisting of a 1 mm thick FR4 support layer coated with a 60 μm copper film that is passivated by a 50 nm gold film. Dimensions of the substrates were 2 cm × 0.5 cm. Prior to electrodeposition, the substrates were cleaned using a sequential immersion process: each sample was dipped for 60 s in 0.1 M hydrochloric acid (HCl, 37%, VWR International, USA). This is followed by rinsing with acetone (VWR International, USA) and isopropyl alcohol (IPA, VWR International, USA). After cleaning, the substrates were dried under a nitrogen stream before use.

Base electrolyte preparation.—The DHBT electrolyte consisted of 0.12 M copper (II) sulfate pentahydrate ($CuSO_4.5H_2O$, >98%, VWR International, USA) and 1.5 M sulfuric acid (H_2SO_4, 96%, BASF, Germany) dissolved in deionized water. This formulation was based on established DHBT literature protocols[18,19] and the same electrolyte concentration was used throughout all experiments to ensure consistency.

Electrolyte additives preparation.—Citric acid (⩾99.5%, VWR International, USA) and hydrochloric acid (37%, VWR International, USA) were used as additives. 0.1 M citric acid and 10 mM HCl were introduced into the base bath either individually or in combination, immediately before deposition. Solutions were stirred magnetically for 10 min to ensure complete mixing. In exploratory experiments, additives that are commonly used in Cu electrodeposition systems were also evaluated at concentrations of 0.01 mM such as

bis-(sodium sulfopropyl)-disulfide (SPS, 97%, Fluorochem, Ireland), Janus Green B (JGB, Sigma-Aldrich, USA), N,N-dimethyl-di-thiocarbamoyl propyl sulfonic acid sodium salt (DPS, 97%, BLD Pharmatech GmbH, Germany), 3-mercapto-1-propane sulfonic acid sodium salt (MPS, 90%, Sigma-Aldrich, USA), 1,2,3-benzotriazole (BTA, 99%, Merck, USA), and dodecyl trimethylammonium chloride (DTAC, 98%, Thermo Scientific, USA).

Electrodeposition process.—Nano-dendritic Cu films were deposited via the DHBT method using both continuous (direct current, DC) and pulsed electrodeposition modes using a programmable power supply (Plating Electronic, Germany). The counter electrode in all settings was a 3 cm × 7 cm platinum-coated titanium mesh. The inter-electrode distance was fixed at 2 cm for all experiments through a custom electrode holder setup. All deposition experiments were executed at room temperature without further active pH adjustment of the bath for a total deposition time of 20 s (unless explicitly stated otherwise). Following electrodeposition, samples were rinsed under running deionized water for 60 s and dried under gently blown nitrogen.

Pulse-assisted electrodeposition was applied using a rectangular on/off waveform. In this mode, the duty cycle (C_{duty}) is defined as the ratio of the "on-time" (T_{on}) to the total pulse cycle duration ($T_{on} + T_{off}$), expressed as a percentage. During the "on" state, a peak current density (J_{peak}) is applied, while no current is supplied during the "off" state. The average current density (J_{avg}) represents the time-averaged current across the full cycle. For a given target J_{avg}, a lower duty cycle requires a proportionally higher J_{peak} so that the time-averaged current over the entire cycle remains equal to the intended J_{avg}. All pulse-deposited samples were produced at a fixed frequency of 50 Hz, corresponding to a total pulse cycle time of 20 ms. Preliminary experiments conducted at lower frequencies (0.5–10 Hz; cycle durations up to 2 s) did not yield significant results and were therefore excluded from further investigation. Table I summarizes the set of process parameters used in this study. For clarity, each sample is labeled based on its deposition conditions throughout the study. For example, the sample "C25J2" will refer to the replicate deposited at a duty cycle of 25% and an average current density of 2.0 A cm^{-2}.

Characterization.— *Film morphology analysis.*—Film morphologies were analyzed using a field emission scanning electron microscope (Zeiss Sigma 300). Resulting SEM images were processed using ImageJ Software (NIH, USA). A detailed overview of how results from this analysis are obtained is shown in Fig. S1. All data points were derived from at least four SEM images obtained from a minimum of two separate, but under identical conditions processed, samples for statistical relevance and reproducibility. Binary thresholding was applied using the automated Otsu thresholding technique,[20] followed by analysis on regions of interest. A general indication of the surface porosity (A_{por}) is given by the open area over total surface area (i.e., area fraction of visually distinguishable macro-pores observed at top surface SEM images). Pore size distribution data was generated using the ImageJ binning function. Subsequently the average pore diameter (D_{avg}) and full width at half maximum of the pore size distribution (D_{FWHM}) was obtained from the fit of a normal distribution to the binned data.

Film thickness.—Film thickness (H_f) measurements were carried out using an optical microscope (Leica Reichert Jung Polyvar MET) equipped with calibrated *z*-axis control. By applying a mechanical scratch through the film layer at two different locations, the thickness was determined by measuring the focus difference between the scratched substrate and the adjacent intact film surface at two distinct points per location. The growth rate of the films (V_f) was calculated by division of the resulting film thickness by the corresponding deposition time.

In-Situ bubble behavior observations.—To observe hydrogen bubble behavior during deposition, high-speed video recordings were captured using a Chronos 1.4 High-Speed Camera (Kron Technologies), equipped with a Computar 12.5–75 mm f/1.2 zoom lens. This setup allowed for in situ observation of dynamic bubble behavior at the cathode surface under different electrolyte and current conditions.

Cross-section analysis.—To examine the bottom to top morphology of the porous Cu films, a selection of relevant samples were prepared for cross-sectional SEM analysis. After electrodeposition, the substrates containing the porous Cu films were mechanically sectioned into two halves using a precision cutting tool to expose the internal structure of the deposits. The cut samples were then mounted vertically on an SEM stub. This configuration enabled direct side-view imaging. Cross-sectional SEM images were acquired under the same operating conditions as the top-view measurements.

Results

Establishing the DHBT process window.—To establish the process window to obtain useful Cu films for this study of the DHBT process, exploratory experiments were performed using 20 s of continuous deposition at J_{avg} of 0.1, 1.0, 1.5 and 2.5 A cm^{-2}. At J_{avg} = 0.1 A cm^{-2} (Fig. 2a), the film surface primarily consists of isolated copper grains and a few laterally collapsed dendritic protrusions, indicating that the applied J_{avg} is insufficient to sustain continuous hydrogen evolution or promote self-supported dendritic growth. Increasing J_{avg} to 1.0 A cm^{-2} (Fig. 2b) initiates more pronounced nucleation and dendrite formation. The round indents of about 50 μm in diameter in the deposit reveal that hydrogen bubbles start shaping the overall morphology, however, most structures remain quite laterally oriented and disconnected as a continuous three-dimensional porous framework has yet to develop. At J_{avg} = 1.5 A cm^{-2} (Fig. 2c), the morphology transitions toward a denser, interconnected network where individual dendrites begin to coalesce into ligament-like domains. Although a porous framework emerges, the underdeveloped pore geometry remains shallow and bowl-shaped, as a result of limited vertical propagation of ligaments. For J_{avg} = 2.5 A cm^{-2} (Fig. 2d), the morphology evolves into a fully developed, self-supporting three-dimensional architecture characterized by multi-layered dendritic ligaments and interconnected pores extending beneath the surface. Therefore, inherent to porous, nano-

Table I. Electrodeposition parameters applied for the duty cycle/current density series.

Deposition			J_{peak} (A/cm^2)				
Mode	T_{on} (ms)	C_{duty} (%)	J_{avg}	1.5	2.0	2.5	3.0
Continuous	—	100		1.5	2.0	2.5	3.0
Pulsed (50 Hz) 20 ms cycle time	15	75		2.0	2.7	3.3	4.0
	10	50		3.0	4.0	5.0	6.0
	5	25		6.0	8.0	10.0	—

Note that in continuous mode (i.e., C_{duty} = 100%) J_{avg} equals J_{peak}. The applied peak current density times the duty cycle equals the average current density of the associated continuous mode reference experiment. The equipment limits the current density J_{peak} to a maximum of 10 A cm^{-2}.

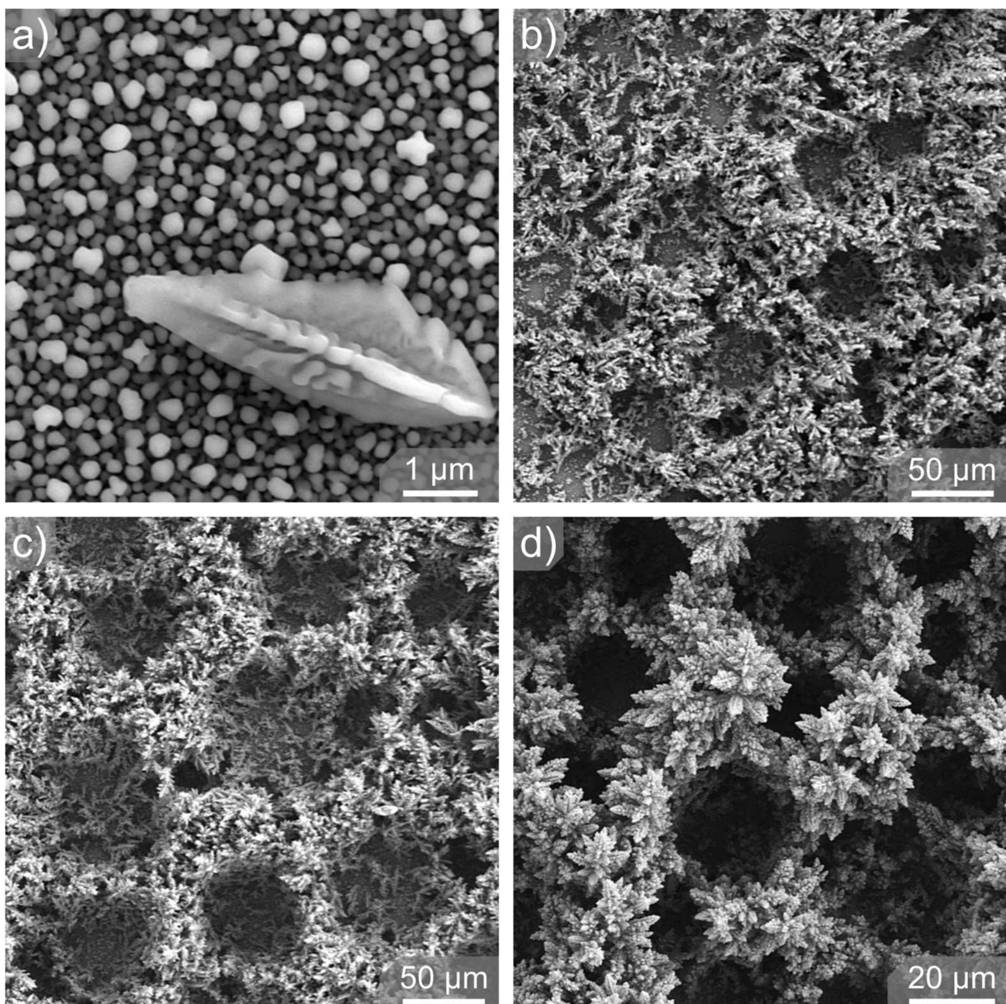

Figure 2. Development stages of the porous nano-dendritic films deposited under continuous deposition at average current densities of (a) 0.1 A cm^{-2}, (b) 1 A cm^{-2}, (c) 1.5 A cm^{-2} and (d) 2.5 A cm^{-2}. With increasing average current density, the electrochemical system is driven further into the mass-transport-limited regime, leading to progressive development of the three-dimensional porous architecture and dendritic branches.

dendritic growth in the DHBT process, the resulting Cu films exhibit significant local morphological variations at the microscale. However, once the current density is sufficiently high (about 1.5 A cm^{-2}), the deposits remain relatively uniform in overall morphology across the full substrate area.

Pulse-assisted additive-free DHBT process.—Under continuous deposition ($C_{duty} = 100\%$), the overall film thickness (H_f) increases nearly linearly with increasing J_{avg}, from approximately 30 μm at 1.5 A cm^{-2} to over 60 μm at 3.0 A cm^{-2}, corresponding to the growth rates (V_f) ranging from ∼1.5 μm s^{-1} to just over 3 μm s^{-1} (Fig. 4a). Despite this increase in growth rate, the large-scale porous morphology of all $C_{duty} = 100\%$ films actually remains quite similar. The SEM image of the sample obtained at $J_{avg} = 2.5$ A cm^{-2} shown in Fig. 3a is therefore representative for all samples produced at $C_{duty} = 100\%$. This observation is sustained by the fact that the quantitative morphology characteristics (surface porosity, average pore diameter and distribution) deduced from the SEM images are fairly constant and do not show a very clear trend as a function of J_{avg} (see Figs. 4b–4d).

The series of pulse deposited samples at $C_{duty} = 25\%$ (Figs. 3b–3d) also display consistent morphology across the J_{avg} range, where the film deposited at $J_{avg} = 1.5$ A cm^{-2} still appears slightly underdeveloped with a single layer of bowl-shaped indentations (as also shown in Fig. 2c) rather than a structure of stacked pores. Nevertheless, just like for $C_{duty} = 100\%$, A_{por}, D_{avg} and D_{FWHM} are fairly constant and do not show a very clear trend as a function of J_{avg} (see Fig. 4b–4d). Similar observations are obtained for the intermediate duty cycles of 50% and 75%. J_{avg} clearly determines the vertical growth rate of the film for which the duty cycle only seems to be a secondary effect (see Fig. 4a), but J_{avg} does not have clear impact on the morphology. This indicates that after an initial nucleation stage, a balance is established in which the non-equilibrium dendritic growth of the ligament structure does not continue to progress out of control. Instead, it is regulated by the periodic nucleation, growth and detachment of the hydrogen bubbles in the DHBT process. On the other hand, experiments demonstrate that, largely independent of J_{avg}, the duty-cycle modulation determines the morphology of porous Cu films. As indicated by Figs. 4c and 4d, reduced duty cycle provides films with smaller and more uniformly distributed pore diameters. That is the morphology refines with decreasing duty cycle. Figure 4b shows that a decreasing duty cycle also results in a reduced porosity of the Cu films, but this effect is less pronounced than for D_{avg} and D_{FWHM}. Although samples produced by pulsed deposition might contain less total deposit of metal (i.e., due to lower thickness), the concurrent reduction of A_{por} indicates the formation of a more compact in-plane network of dendritic walls and ligaments. To ensure that the observed refinement upon pulsed deposition is not merely a consequence of reduced film thickness, a comparative analysis was conducted between samples of similar thickness. Specifically, a C25J2.5 sample deposited for 20 s yielded a film thickness of approximately ∼35 μm,

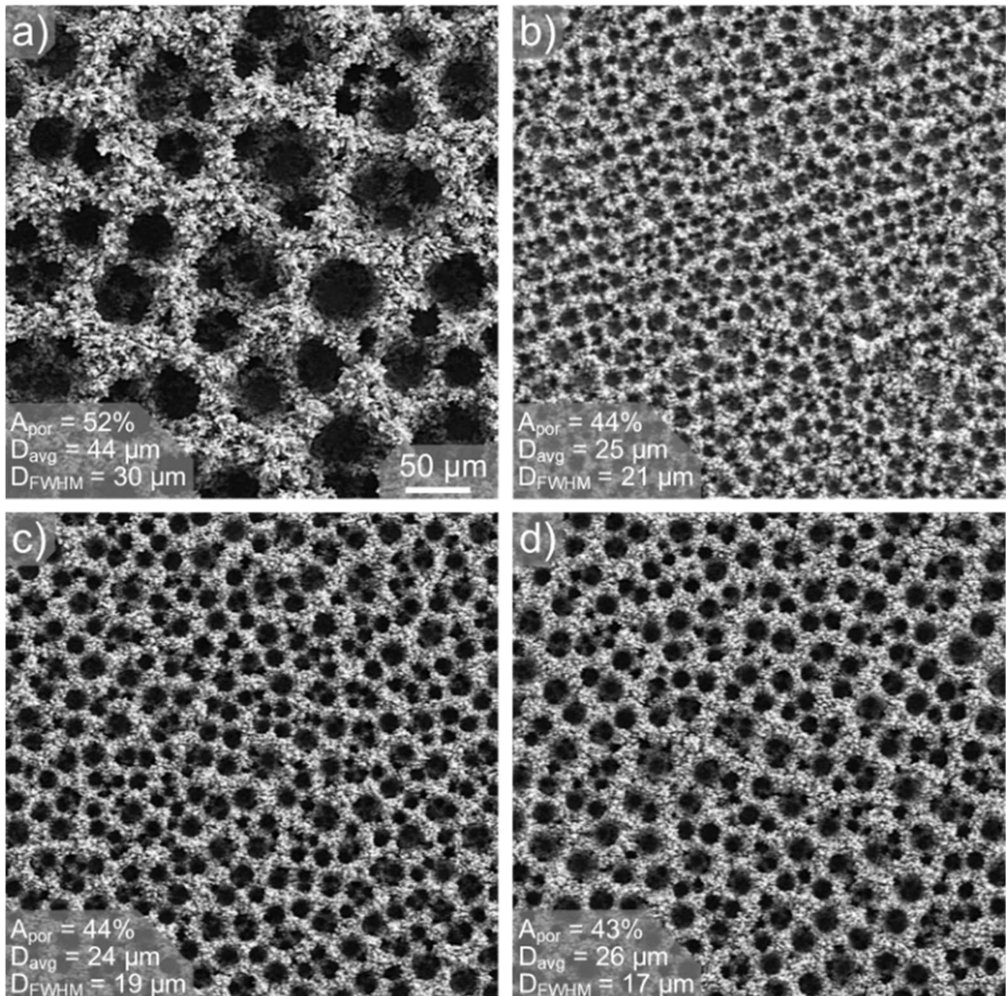

Figure 3. Top-view SEM images of porous nano-dendritic copper films deposited at a fixed frequency of 50 Hz under varying average current densities (J_{avg}) and duty cycles (C_{duty}). (a) Continuous deposition ($C_{duty} = 100\%$) at $J_{avg} = 2.5$ A cm^{-2}. (b)–(d) Pulsed deposition ($C_{duty} = 25\%$) at $J_{avg} = 1.5$ A cm^{-2}, 2.0 A cm^{-2}, 2.5 A cm^{-2}, respectively. All images are on the same scale.

while a C100J2.5 sample deposited for 15 s produced a comparable thickness. Despite this similarity in thickness, the C25J2.5 sample displays a significant reduction in average pore diameter by at least a factor of two (Fig. S2). This indicates that the morphological refinement observed under pulsed conditions arises primarily from the transient electrochemical environment created rather than from changes in total deposition volume.

Figure 5 presents SEM images of the overall branch structures and the more detailed morphology of the individual dendrites of films deposited at a J_{avg} of 2.5 A cm^{-2} at $C_{duty} = 100\%$ (Figs. 5a and 5b) and pulsed current conditions at $C_{duty} = 25\%$ (Figs. 5c and 5d). The images show structures consisting of stems pointing in different directions that are decorated with rows of protrusions in rather well-defined directions. This indicates that there is a crystallographic connection between each stem and its protrusions typical for dendritic growth of crystals. The growth mode is determined by rapid incorporation of growth units at the growing surface such that the transport of units from the medium towards the growing surface limits the deposition rate. The tip of the stems grows fastest taking up all locally available growth units thus leaving a depleted electrolyte solution for a series of smaller protrusions positioned just below the top. At a certain distance from the top, the concentration of growth units is again sufficient to allow some individual protrusions to expand rapidly into a branch with protrusions of its own. The pulse deposited samples show significantly smaller stems that are branched at a much smaller distance from their top, resulting in a more finely structured deposit having an estimated reduction in branch size by approximately a factor of four.

Effect of additive chemistry on nano-dendritic copper films.—It is well-known that the electrodeposition process can be tailored by incorporating trace amounts of electrolyte additives, which are widely used in conventional copper electrodeposition to influence growth kinetics and deposit morphology.[21,22] Common copper plating additives such as accelerators (e.g., SPS, MPS, DPS), suppressors (e.g., PEG + Cl^{-}), and other agents (e.g., JGB, BTA, DTAC) typically act by adsorbing selectively on surfaces and modifying the local deposition rate, as well as refining the grain structure.[23–25] Motivated by this established strategy, we initially explored the effect of introducing very low concentrations (0.01 mM) of some of these common additives into the deposition bath, at $C_{duty} = 100\%$ and $J_{avg} = 2.5$ A cm^{-2}. SEM analysis showed that, at least at the low concentrations tested, these additives did not produce significant modifications in the porous morphology and dendritic branch structures remained largely similar to those shown in Fig. 5. Representative SEM images are provided in Figs. S3 and S4.

While previous studies have shown that some of the above-mentioned additives (e.g., BTA) can alter morphology at higher concentrations,[26] it was decided to focus this study on exploring alternative additives that could more directly influence the DHBT mechanism. For this purpose, two additives were selected with

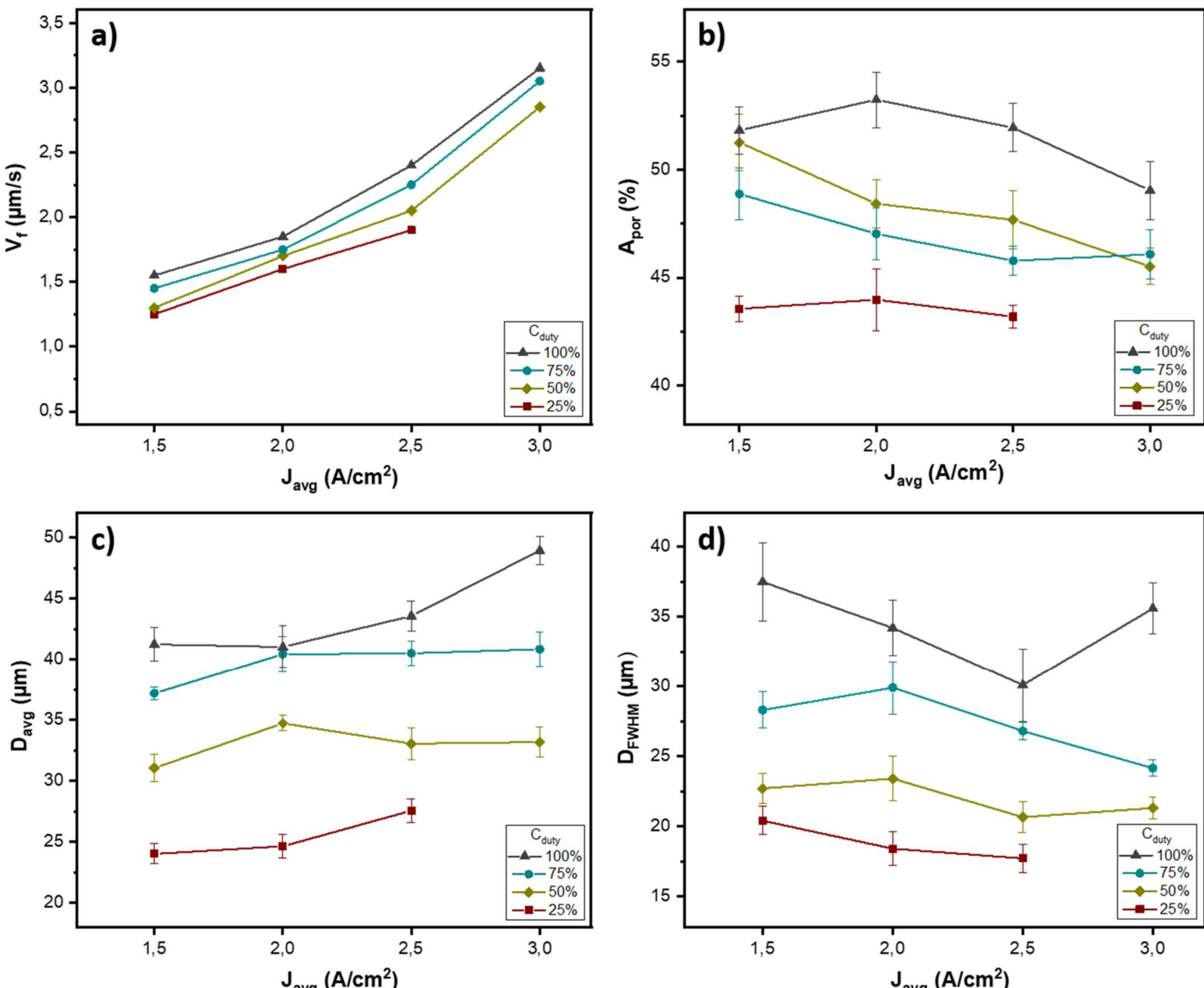

Figure 4. Variation of (a) film growth rate (V_f), (b) surface porosity (A_{por}), (c) average pore diameter (D_{avg}) and d) full width at half maximum of the pore size distribution (D_{FWHM}) as a function of average current density for continuous and pulsed deposition. Different colors and symbols correspond to duty cycles of C_{duty} = 100%, 75%, 50% and 25%. Lines are simply connection of the data points.

mechanistic relevance to the DHBT. Citric acid, an organic agent that can be used for modulation of hydrogen bubble dynamics and chloride ions, known to influence growth mechanism by accelerating copper reduction in the electrodeposition system.[27,28] In a comparative study the influence of these selected additives on the porous architecture of nano-dendritic copper films is evaluated. The case with no-additive (denoted as "Base") serves as a baseline reference for comparing the films deposited in the presence of citric acid (denoted as CA), chloride ions (from HCl), and their combination (CA + HCl), under both continuous (C_{duty} = 100%) and pulsed (C_{duty} = 25%) deposition conditions for 20 s.

Figure 6 shows high-speed camera images obtained during the continuous electrodeposition process. These images correspond to the early stage of the deposition process, as at later stages the rapid evolution and detachment of hydrogen bubbles obscure the surface, preventing clear visualization. Consequently, bubble detachment appears more pronounced near the sample edges, where the local electrolyte flow facilitates earlier bubble release compared to the central region. For the additive-free (Fig. 6a) and HCl (Fig. 6c) cases, the hydrogen bubble distribution over the growing Cu films are fairly similar with clearly identifiable attached rows of bubbles in the center of the sample and larger detaching bubbles at the edges. The situation is entirely different for deposition experiments that include CA as an additive. In these cases, the entire sample surface is covered with a high density of small hydrogen bubbles. Instead of larger bubbles, a mist of smaller detaching bubbles is observed in particular at the edges of the samples. The characteristics of the resulting porous nano-dendritic Cu films are shown in Figs. 7 and 8.

When citric acid is introduced (Fig. 7a), the resulting porous structure upon continuous deposition is about 20% smaller and about 40% more uniformly distributed compared to the corresponding film formed without additives (Fig. 3a). Figure 8 further shows that the film thickness (H_f) of both samples is virtually the same and that also the surface porosity does only differ about 10%. Compared to continuous deposition with CA, pulsed deposition (Fig. 7d) shows the usual refinement in morphology, accompanied by a decrease in surface porosity from 47% to 42%. In comparison to pulsed deposition without CA, the most striking difference is the strongly increased uniformity in pore size distribution (about 40% reduction in D_{FWHM}) while the other film properties are highly comparable (less than 10% difference). Apparently, the conditions for which hydrogen bubbles detach from the growing film surface are sharper defined in the presence of CA. Overall, compared to the additive free conditions, the introduction of CA results in a smaller average pore diameter and significantly more uniform pore distribution. Thus, the introduction of CA and the application of on/off pulses both lead to a

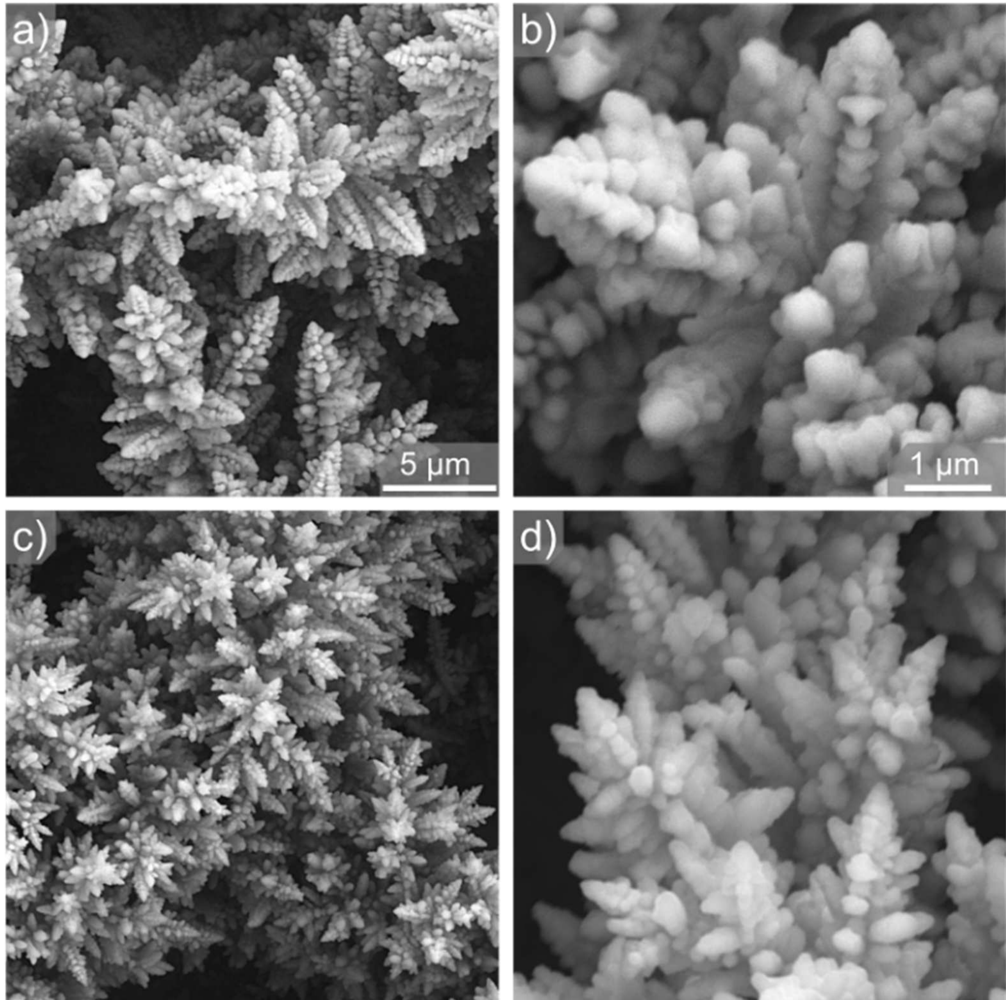

Figure 5. SEM images at different magnifications showing nano-dendritic copper branch morphology deposited at an average current density of $J_{avg} = 2.5$ A cm^{-2}. Images (a) and (b) correspond to continuous deposition ($C_{duty} = 100\%$), while (c) and (d) correspond to pulsed deposition ($C_{duty} = 25\%$). Images (a) and (c), as well as (b) and (d), are on the same scale.

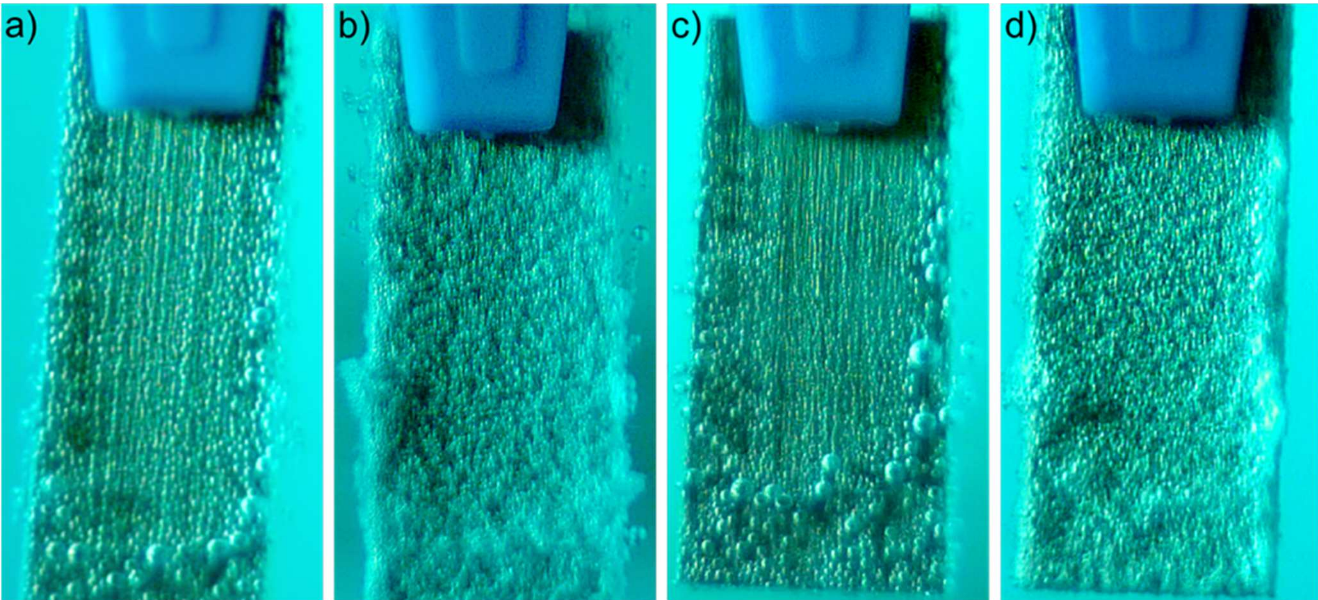

Figure 6. High-speed camera images of the cathode surface captured during the continuous deposition process ($C_{duty} = 100\%$, t ~ 100 ms after current application). Images correspond to electrolyte baths containing (a) no additives (base), (b) citric acid (CA), (c) chloride ions (HCl) and (d) combined CA + HCl. The images illustrate differences in hydrogen bubble nucleation density and detachment behavior at the cathode surface.

Figure 7. Top-view SEM images of porous nano-dendritic copper films deposited at $J_{avg} = 2.5$ A cm^{-2} and $C_{duty} = 100\%$ (upper row) or $C_{duty} = 25\%$ (lower row) with electrolyte solutions containing different additives. (a) and (d) Citric acid (CA), (b) and (e) chloride ions (HCl), (c) and (f) combined CA + HCl. All images are on the same scale.

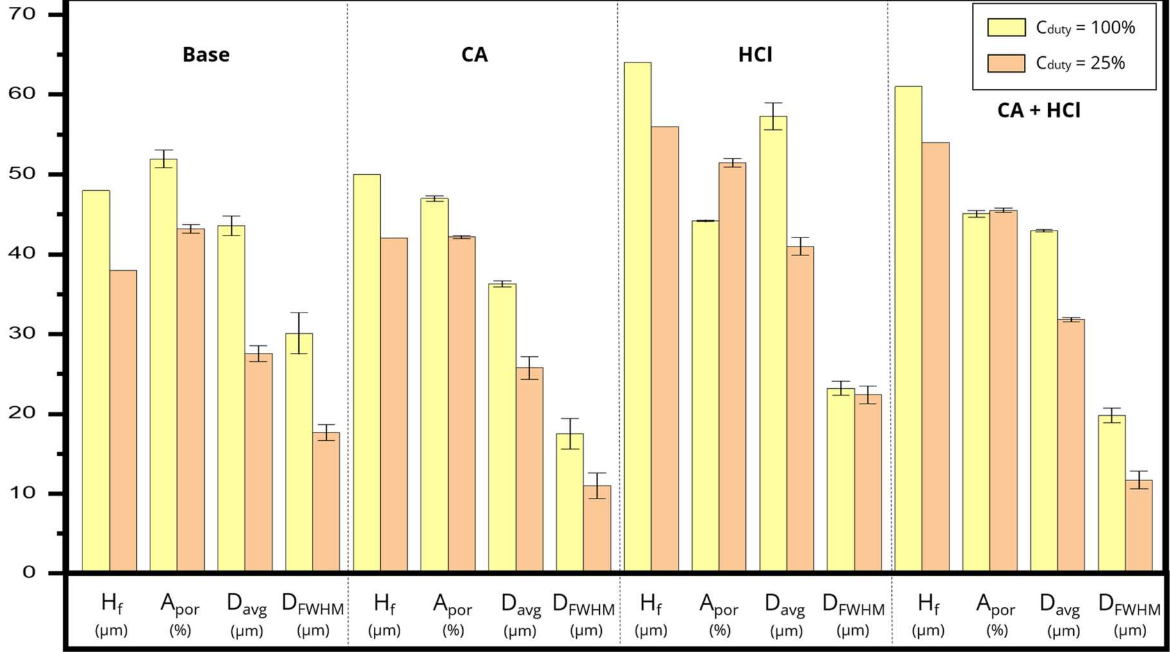

Figure 8. Variation of film thickness (H_f), surface porosity (A_{por}), average pore diameter (D_{avg}) and full width at half maximum of the pore diameter distribution (D_{FWHM}) under continuous deposition ($C_{duty} = 100\%$) and pulsed deposition ($C_{duty} = 25\%$) conditions. Data are shown for the electrolyte solutions containing no additives (base), citric acid (CA), chloride ions (HCl) and combined CA + HCl.

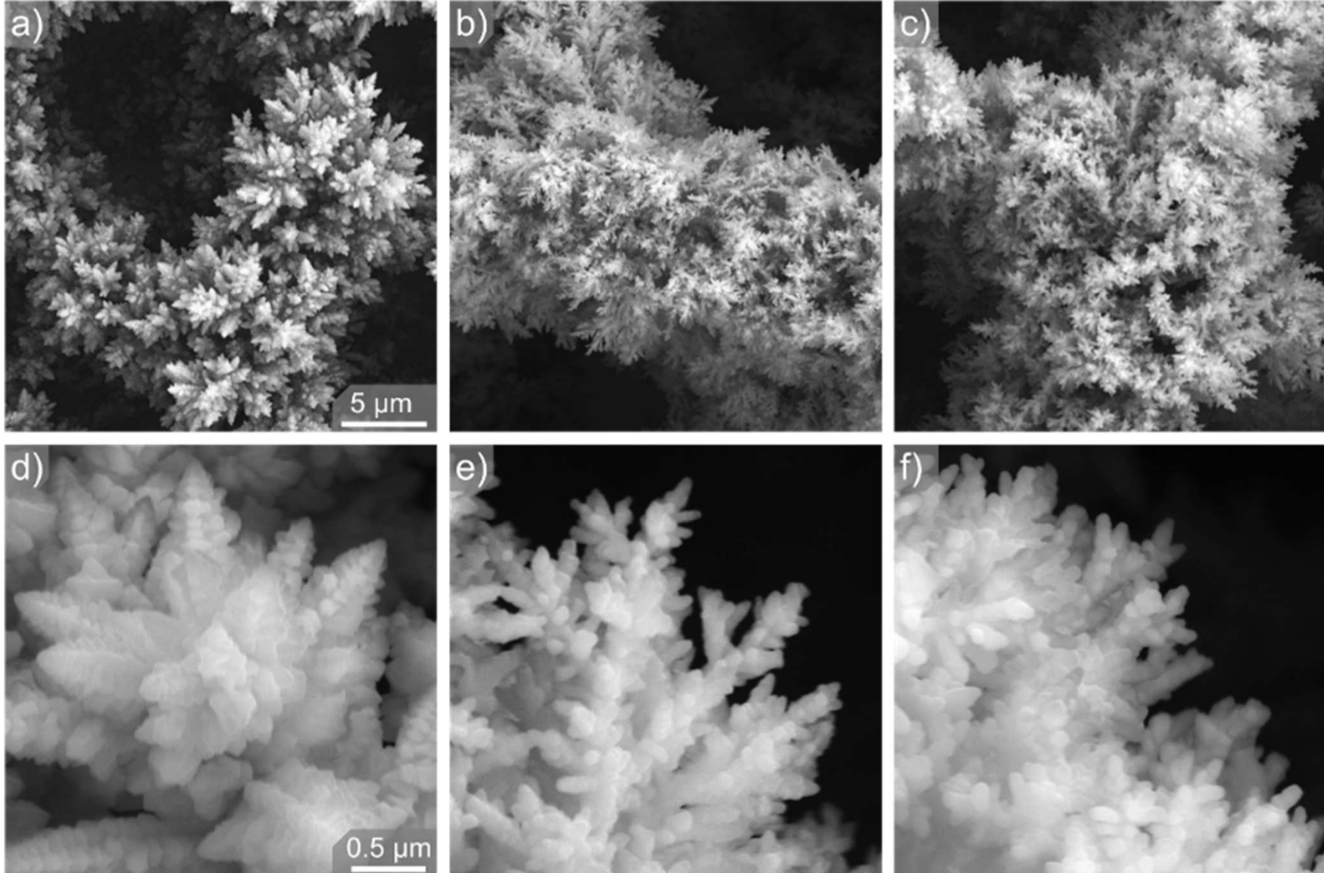

Figure 9. High-magnification SEM images of nano-dendritic copper branches deposited at $J_{avg} = 2.5$ A cm^{-2} with electrolyte solutions containing different additives. Upper row: (a) Citric acid (CA), (b) chloride ions (HCl), (c) combined CA + HCl. Lower row: (d) CA (e) HCl, (f) CA + HCl. Images within each row are shown at the same scale.

refinement of the film morphology, without altering its basic structure. In contrast, the addition of HCl to the deposition process provides a genuine change in the porous structure of the film (see Fig. 7b). The morphology shifts toward large, elongated, ellipsoid-like pores separated by rather smooth, thick walls that dominate the structure. When a pulsed condition is applied in the HCl system (Fig. 7e), the pores become smaller (57 µm vs 41 µm), while the walls are thinner and also obtain a much rougher appearance again (comparing the appearance of the pore walls in Fig. 7a with that of 7b and 7c). This results in a more open, higher-void-fraction network as also reflected in the increase in surface porosity from 44% to 51%. Furthermore, Fig. 8 shows that compared to the additive-free case, the addition of HCl yields a significant increase in growth rate of about 25% and 50% for continuous and pulsed deposition, respectively.

When CA and HCl are combined, the resulting structures reflect contributions from both additives. Under continuous deposition (Fig. 7c), the pore shape remains similar to that obtained with HCl alone, yet pores are smaller, and walls are thinner, suggesting that CA partially counteracts the strong wall-thickening and pore-enlarging effects of Cl^-. Upon pulsed deposition (Fig. 7f), the porous network refines again, as pores become more circular and smaller (43 µm vs 32 µm). Actually, the D_{avg} for CA + HCl is almost exactly in between those of CA and HCl alone, both for continuous and pulsed deposition. In contrast, Fig. 8 shows a decrease in D_{FWHM} relative to Cl^- only system but similar to the CA only system, confirming that CA acts as the dominant additive controlling pore size modulation. The relatively unchanged A_{por} in the combined additive system (Fig. 8) suggests a balance between wall thinning and structural preservation, yielding a refined yet coherent porous framework. Film thickness measurements further support these observations. The combined CA + HCl system results in thicknesses similar to the HCl-only case (~60 µm) confirming that HCl accelerates the deposition process. In all additive-containing systems, pulsed deposition at $C_{duty} = 25\%$ leads to an ~8–10 µm decrease in thickness compared to $C_{duty} = 100\%$, in line with the trend observed in the additive-free system.

For additive-free conditions the introduction of pulsed deposition did not result in fundamental differences in the nano-dendritic branch structures, instead they are highly similar but smaller than those obtained with continuous deposition (see Fig. 5). A similar result is obtained for all additives examined in this study. Pulsed deposition results in essentially the same morphology of the nano-dendrites but slightly smaller features than observed for continuous deposition. Therefore, we will only discuss the differences in these structures upon addition of CA, HCl and CA + HCl for pulsed deposition (see Fig. 9).

When citric acid (CA) was introduced (Figs. 9a and 9d), the branch structure of the films appears visibly thinner and shorter compared to the additive-free baseline. A distinctly different nano-scale branch morphology emerges with the introduction of chloride ions (Figs. 9b and 9e). Instead of the columnar dendrites with evolving branches that are epitaxially related to their parent trunk found for the additive-free system, the observed copper film consists of disordered laterally extended fractals without apparent epitaxial symmetry. This lateral spreading reflects a transition from anisotropy-driven columnar growth to a more isotropic branching that is typically associated with diffusion limited aggregation (DLA).[29,30] In the combined CA + HCl system (Figs. 9c and 9f), the branch morphologies remained similar to those produced with HCl alone, indicating that Cl^- remains as the dominant branch structuring agent, even in the presence of CA.

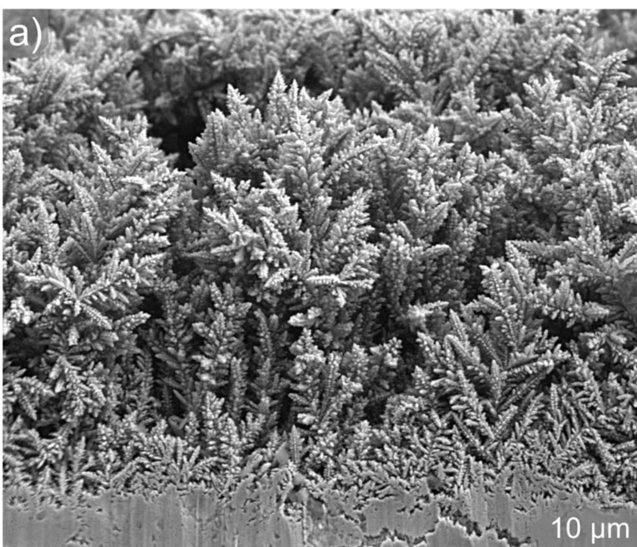

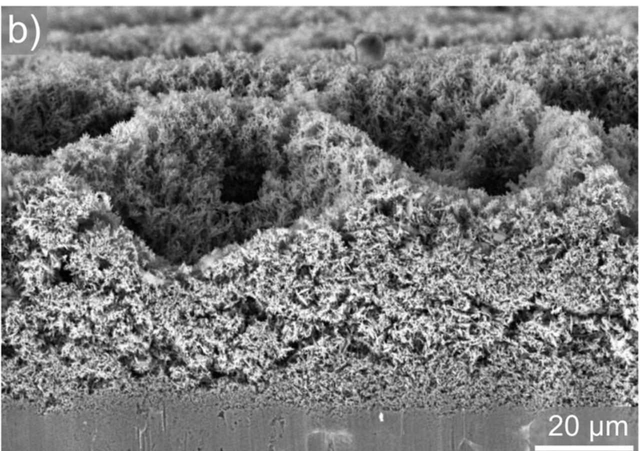

Figure 10. Representative cross-sectional SEM images of porous nano-dendritic Cu films deposited at $J_{avg} = 2.5$ A cm^{-2} for (a) additive-free system and (b) CA + HCl system. The images show differences in ligament architecture and branch organization through the film thickness.

Cross-section analysis.—To further support the morphological distinction observed in the top-view SEM images, cross-sectional SEM images of films representing either side of the morphology range encountered in this work are presented in Fig. 10. Both samples are produced at $J_{avg} = 2.5$ A cm^{-2}. Figure 10a shows a sample produced under continuous deposition without the use of additives resulting in dendritic structures that facilitated by protrusion in the electrolyte and associated increasing uptake of growth units, formed large outward pointing back-bones. Top-view images of films produced under the same conditions are shown in Figs. 2d and 3a. Note that, although the basic morphology is the same, the average length of the dendritic backbones increasingly significant from the bottom (1 μm range) to the top (10 μm range) of the sample. The large outward pointing dendrites on the pore walls at the top of the film almost fully obstruct the vision on the pore cavities.

Figure 10b shows the cross-section of a film with the most refined nanostructure of this study as obtained by the combination of pulse deposition ($C_{duty} = 25\%$) and the use of additives (CA + HCl). Top-view images of films produced under the same conditions are shown in Figs. 7f, 9c and 9f. As stated before, the basic morphology of nanostructures in this film are more fractal-like and distinctly different from the columnar grown dendrites of the film shown in Fig. 10a. Also, the bottom to top increase in the typical feature size is much less pronounced. Even at the top the typical size of the fractal branches are in the 1 μm range. This results in relatively smooth pore walls, providing a good view on multiple upper pore cavities of the film. These cross-sectional images show that the structural differences are intrinsic to the three-dimensional network rather than limited to surface features.

Results and Discussion

In both continuous and pulsed DHBT systems, once the J_{avg} is sufficiently high to drive Cu deposition into the mass-transport-limited regime, the process yields the characteristic formation of dendritic structures (see Figs. 2 and 10a). However, the introduction of pulsed current modulates the deposition dynamics that leads to the demonstrated morphological refinement. During the "on" phase, dendrites form due to rapid Cu^{2+} consumption, but the subsequent "off" period allows for local ion replenishment and relaxation of concentration gradients near the electrode surface.[31] This recovery phase reduces the severity of ion depletion and formation of elongated dendritic structures, thus, promoting the formation of finer, more compact branches. In parallel, these off-times enhance hydrogen bubble detachment, preventing excessive bubble coalescence and thus contributing to smaller, more uniformly distributed pore templates. On the other hand, the average current density, which governs the total amount of charge passed over time, primarily influences the net copper deposition rate and overall film thickness. While J_{avg} governs the total charge input, pulsed samples are observed to be slightly but consistently thinner than their continuous counterparts at the same J_{avg} and deposition time. Although continuous and pulsed deposition at the same J_{avg} involve identical total charge, the instantaneous current partitioning between Cu deposition and hydrogen evolution is not necessarily identical and in principle could lead to quite different morphologies of the resulting films. The fact that we do observe a refinement of the nanostructures but only minor structural differences in film geometry between the two growth modes might be seen as an indication that the split of charge for Cu deposition and H_2 generation is actually quite similar under continuous and pulsed deposition. Another more plausible explanation might be that in the additive-free DHBT regime the macro-scale pore framework is governed predominantly by the time-integrated hydrogen bubble nucleation, growth, coalescence, and detachment dynamics, rather than by instantaneous current efficiency alone. Consequently, similar bubble behavior over the full deposition period can yield comparable large-scale porosity, even if the transient Cu/H_2 current distribution differs. Overall, the results presented demonstrate the role of pulsed deposition as a tool in the DHBT system that enables morphological control through transient effects.

The effects of citric acid (CA) in the DHBT system can be described through its influence on hydrogen bubble dynamics during deposition. In CA-containing electrolytes, the nucleation density of hydrogen bubbles is significantly higher, as visible in the high-speed imaging (see Fig. 6), where the surface is populated by many small bubbles rather than the larger bubbles observed in the additive-free or Cl-only systems. It is reasonable to assume that bubble detachment often occurs when adjacent bubbles grow and coalesce to exceed the adhesion threshold, therefore, a high nucleation density naturally restricts the lateral growth of individual bubbles, leading to earlier detachment and smaller effective bubble templates. A contributing factor to the elevated nucleation density may be the ability of protonated citrate species to participate in hydrogen evolution through direct discharge of hydrogen atoms bound within the molecule.[27] As reported by Marinovic et al.,[27] this pathway becomes increasingly active at lower pH, which is relevant for the strongly acidic conditions of the present DHBT system (pH < 1). As a result, the reduced pore sizes and narrower pore-size distributions are observed for CA-containing films. Although these refinements are primarily attributed to enhanced hydrogen bubble dynamics, citrate adsorption at the Cu surface may also be a contributing factor to the observed effects. At present, no direct literature evidence clearly confirms such adsorption under strong hydrogen-evolving

conditions, and experimental verification in this regime is inherently challenging.

As shown in previous studies, Cl^- ions act as catalytic ligands in the copper electrodeposition system that facilitates a faster copper reduction through an inner-sphere complexation mechanism, typically yielding finer nanostructures.[28,32,33] Also, within the DHBT system, the presence of Cl^- appears to have a significant impact on the growth mechanism of the Cu nanostructures making up the ligaments between the pores. In the additive-free DHBT system Cu growth yield straight columnar dendrites that below their tip progressively develop periodic rows of knobs at their side as shown in Figs. 5b and 5d. These knobs are well-defined and symmetrically distributed around the central column and develop in branches under specific inclinations as a result of the growth asymmetry dictated by the Cu crystal lattice (i.e., the central column and the branches have an epitaxial relation).[30] Over time the individual branches also evolve into branched columnar dendrites themselves. The overall structure of the ligaments is governed by the growth competition between these dendrites yielding a relatively dense arrangement of inter-twinned columnar structures. There where the dendrites experience less mutual competition at the outer edge of the ligaments and at the initial growth stage, the central column typically is allowed to extend further into the medium. Instead of having a straight central column, the nanostructures grown upon Cl^- addition have a more disordered fractal appearance with randomly distributed branching (see Figs. 9b and 9e). In early studies on electrodeposition such disordered fractal morphologies were associated with a growth process referred to as diffusion limited aggregation (DLA).[29,30] Crystallization studies indicated that this change in morphology can be explained by the cross-over from crystal anisotropy driven stable growth of the columnar tip to unstable tip splitting and loss of the epitaxial relation under more isotropic crystal growth conditions.[30,34] In successive studies, several specific non-dendritic fractal structures were distinguished that were referred to as dense branching morphology (DBM)[35,36] or seaweed growth,[37,38] homogeneous, open and finger-like fractal structures.[39,40] Whereas these previous studies typically describe millimeter sized fractal structures obtained in quasi-two-dimensional electrodeposition experiments, the application of DHBT in the present study demonstrated a similar cross-over from an ordered dendritic to a disordered fractal morphology. However, the present work shows structures on a micrometer scale with on one hand clear dendrites and on the other hand specific additive induced disordered fractals that might be best described as fractal-like DBM.[35,36] The tips of the fractal-like DBM do not experience the increasingly accelerated growth that make the backbone of dendrites increasingly protrude into the electrolyte during growth. As a consequence, the ligaments making up the porous Cu structures grown with HCl additives in particular have a very smooth appearance as is also clearly visible in the cross-section of Fig. 10b.

From the application perspective, the films with refined structures shown in this study are directly aligned with the functional requirements of nanostructured Cu interfaces that can be used in diffusion-driven bonding and related high-performance electronics packaging applications.[14] As highlighted earlier, interfaces that combine reduced macro-porosity with a dense network of fine ligaments are particularly advantageous for achieving rapid solid-state consolidation and efficient mass transport during bonding. The structural tuning achieved here (i.e., smaller and more uniformly distributed pores, more compact branch networks) addresses precisely these requirements. As reported in a separate study by our group,[41] bonding trials performed using the films fabricated in the present work also confirmed that these tailored morphologies support rapid consolidation and continuous bonded areas with comparable bondline properties (vs commercially available powders/pastes) under practical package assembly conditions. Continued efforts toward interface consolidation studies and reliability assessments will be essential for fully establishing their performance, but the pathways for structural control identified here provide a clear foundation for advancing these materials toward application-ready technologies.

Conclusions

In this study, the morphological tuning of porous nano-dendritic copper films produced by the dynamic hydrogen bubble templating (DHBT) method with pulse duty cycle modulation and targeted additive chemistry was systematically investigated. In-situ observations of the process using a high-speed camera combined with the detailed post-deposition SEM analysis of the resulting nano-porous Cu films provided insights to the hydrogen bubble templating and Cu growth mechanisms that determine the final morphology of the films. It has been demonstrated that modulation of the duty cycle from continuous deposition (100%) to pulsed deposition (25%) refined the porous network, yielding smaller pores, narrower pore size distributions, and more compact dendritic architectures. Selected electrolyte additives also provided an effective pathway for structural control. Citric acid influenced the macro-scale porosity by promoting finer, more uniformly distributed pores and shortening branch dimensions through its role in hydrogen bubble dynamics. Chloride ions, by contrast, showed a dominant influence at the branch level, accelerating copper reduction and shifting growth from multidirectional dendrites toward elongated fractal-like structures. When both additives were combined, each retained its dominant role, citric acid controlling macro-porosity and chloride ions controlling branch morphology, producing a refinement mechanism of the overall film morphology. Pulsed deposition was found to offer this dual-additive system an additional degree of tunability; however, it showed a more subtle effect compared to the additive-free case. As such, pulse-assisted deposition can be viewed as an optional tool in additive-containing systems, rather than a dominant structure control mechanism. Overall, this work expands the understanding on the investigated tools that could be useful for tailoring nano-dendritic Cu architectures via scalable electrochemical routes and highlights pathways for optimizing these structures to be employed in various advanced technological domains.

Acknowledgments

Funding: This study was carried out under project number P20–13 (Circular Circuits) in the framework of the Partnership Program of the Materials Innovation Institute M2i (www.m2i.nl) and the Netherlands Organization for Scientific Research (www.nwo.nl). Authors would like to thank Radboud UMC RTC Microscopy Center for use of facilities. Authors would like to thank Radboud University Physics Practical Laboratory for use of high-speed camera. The graphical abstract was created using BioRender.com and adapted with original SEM images.

ORCID

Fatin Battal https://orcid.org/0000-0003-3685-4238
Nikhil Gupta https://orcid.org/0009-0000-7922-2703
Peter Mulder https://orcid.org/0009-0004-5092-9878
Jeroen Maasen https://orcid.org/0009-0001-6637-7332
René H. Poelma https://orcid.org/0000-0002-4180-7033
Elias Vlieg https://orcid.org/0000-0002-1343-4102
John J. Schermer https://orcid.org/0000-0002-6004-7906

References

1. L. -P. Lefebvre, J. Banhart, and D. C. Dunand, "Porous metals and metallic foams: Current status and recent developments." *Adv. Eng. Mater.*, **10**, 775 (2008).
2. K.-R. Yeo, J. Eo, M. J. Kim, and S.-K. Kim, "Shape control of metal nanostructures by electrodeposition and their applications in electrocatalysis." *J. Electrochem. Soc.*, **169**, 112502 (2022).
3. A. Dutta, M. Rahaman, N. C. Luedi, M. Mohos, and P. Broekmann, "Morphology matters: Tuning the product distribution of CO_2 electroreduction on oxide-derived Cu foam catalysts." *ACS Catal.*, **6**, 3804 (2016).
4. S. H. Jung and J.-H. Lee, "Ultrafine dendritic Cu particles for extremely fast pressure-assisted sintering under air and pore-free bond lines." *Journal of Materials Research and Technology*, **35**, 3045 (2025).
5. S. Vesztergom, A. Dutta, M. Rahaman, K. Kiran, I. Zelocualtecatl Montiel, and P. Broekmann, "Hydrogen bubble templated metal foams as efficient catalysts of CO_2 electroreduction." *ChemCatChem*, **13**, 1039 (2021).

6. G. Janod, L. Chachay, J. Schoenleber, Y. Avenas, D. Bouvard, R. Daudin, J.-M. Missiaen, M.-P. Gigandet, J.-Y. Hihn, and R. Khazaka, "Evaluation of thermocompressed nanoporous copper deposit to replace soldering for power electronic metal foam heat sinks." *IEEE Trans. Compon., Packag. Manufact. Technol.*, **14**, 1359 (2024).
7. B. J. Plowman, L. A. Jones, and S. K. Bhargava, "Building with bubbles: the formation of high surface area honeycomb-like films via hydrogen bubble templated electrodeposition." *Chem. Commun.*, **51**, 4331 (2015).
8. H.-C. Shin, J. Dong, and M. Liu, "Nanoporous structures prepared by an electrochemical deposition process." *Adv. Mater.*, **15**(19), 1610-1614 (2003).
9. M. Das, A. Biswas, T. Purkait, T. Boruah, S. Bhardwaj, S. K. Das, and R. S. Dey, "The versatility of the dynamic hydrogen bubble template derived copper foam on the emerging energy applications: Progress and future prospects." *J. Mater. Chem. A*, **10**, 13589 (2022).
10. C. Kharbachi, T. Tzedakis, and F. Chauvet, "Crossover between Re-nucleation and dendritic growth in electrodeposition without supporting electrolyte." *J. Electrochem. Soc.*, **168**, 072507 (2021).
11. J.-H. Han, M. Wang, P. Bai, F. R. Brushett, and M. Z. Bazant, "Dendrite suppression by shock electrodeposition in charged porous media." *Sci. Rep.*, **6**, 28054 (2016).
12. J. Liu, L. Han, X. Zhong, H. Diao, F. Wang, F. Chen, Z. Sun, H. Chen, and H. Zhao, "A novel thermal interface materials based on porous metal copper filled tin for die attachment in power device packaging." *25th International Conference on Electronic Packaging Technology (ICEPT)*1 (2024).
13. J. Wen, J. Su, C. Wang, S. Lu, L. Wang, and W. Zhu, "Novel copper foam/indium composite thermal interface materials for advanced flip chip ball grid array packaging." *25th International Conference on Electronic Packaging Technology (ICEPT)*1 (2024), .
14. F. Battal, D. Boss, R. H. Poelma, E. Vlieg, and J. J. Schermer, "Advancements in TLP bonding for power electronics die-attach applications." *Adv Materials Technologies*, **11**, e01166 (2025).
15. E. Byeol Choi and J.-H. Lee, "Tens-of-seconds solid-state sinter-bonding technique in air using in situ reduction of surface oxide layers on easily bendable dendritic Cu particles." *Appl. Surf. Sci.*, **580**, 152347 (2022).
16. J.-H. Kim, H. Tatsumi, and H. Nishikawa, "Sintered Cu-to-Cu joints using Cu dendritic structure formed by a dynamic hydrogen bubble template with cetyltrimethylammonium bromide." *International Conference on Electronics Packaging and iMAPS All Asia Conference (ICEP-IAAC)*197 (2025).
17. J.-H. Kim, H. Tatsumi, and H. Nishikawa, "Direct formation of Cu nano-dendritic structure on substrate by dynamic hydrogen bubble template for organic-free sintered Cu-to-Cu bonding." *Surfaces and Interfaces*, **62**, 106268 (2025).
18. A. Mularczyk, D. Niblett, A. Wijpkema, M. P. F. H. L. Van Maris, and A. Forner-Cuenca, "Manufacturing free-standing, porous metallic layers with dynamic hydrogen bubble templating." *Adv. Materials Inter.*, **11**, 2400052 (2024).
19. Y. Jia, W. Sun, Z. Bai, E. Liu, L. Du, H. Cai, J. Zhang, X. Peng, and L. Wang, "Microstructure and properties of porous copper foils with high specific surface area prepared by electrodeposition." *J. Electrochem. Soc.*, **170**, 083509 (2023).
20. N. Otsu, "A threshold selection method from gray-level histograms." *IEEE Trans. Syst. Man Cybern.*, **9**, 62 (1979).
21. S. P. Wang, K. X. Wei, W. Wei, Q. B. Du, and I. V. Alexandrov, "Enhancing surface roughness and tensile strength of electrodeposited copper foils by composite additives." *Physica Status Solidi (a)*, **219**, 2100735 (2022).
22. M. Paunovic and M. Schlesinger, *Fundamentals of Electrochemical Deposition* (Wiley-Interscience, Hoboken, N.J.) (2006).
23. J. Huang, N. Song, M. Chen, Y. Tang, and X. Fan, "Electrodeposition, microstructure and characterization of high-strength, low-roughness copper foils with polyethylene glycol additives." *RSC Adv.*, **14**, 38268 (2024).
24. J. J. Kelly, C. Tian, and A. C. West, "Leveling and microstructural effects of additives for copper electrodeposition." *J. Electrochem. Soc.*, **146**, 2540 (1999).
25. H. Wang, J. Hu, K. Li, Y. Wang, F. Zhang, and H. Wang, "Effect of additives on the direct electrodeposition of copper from acid solution containing 20 g/l copper (II)." *Int. J. Electrochem. Sci.*, **16**, 150954 (2021).
26. D. Nam, R. Kim, D. Han, J. Kim, and H. Kwon, "Effects of (NH4)2SO4 and BTA on the nanostructure of copper foam prepared by electrodeposition." *Electrochim. Acta*, **56**, 9397 (2011).
27. V. Marinović and A. R. Despić, "Hydrogen evolution from solutions of citric acids." *J. Electroanal. Chem.*, **431**, 127 (1997).
28. H.-C. Shin and M. Liu, "Copper foam structures with highly porous nanostructured walls." *Chem. Mater.*, **16**, 5460 (2004).
29. T. A. Witten and L. M. Sander, "Diffusion-limited aggregation, a kinetic critical phenomenon." *Phys. Rev. Lett.*, **47**, 1400 (1981).
30. D. Grier, E. Ben-Jacob, R. Clarke, and L. M. Sander, "Morphology and microstructure in electrochemical deposition of zinc." *Phys. Rev. Lett.*, **56**, 1264 (1986).
31. B. Qin et al., "Effect of pulse electrodeposition process on the microstructure and properties of electrolytic copper foil as anode current collectors." *Electrochim. Acta*, **528**, 146278 (2025).
32. Z. Nagy, J. P. Blaudeau, N. C. Hung, L. A. Curtiss, and D. J. Zurawski, "Chloride ion catalysis of the copper deposition reaction." *J. Electrochem. Soc.*, **142**, L87 (1995).
33. R. Bakthavatsalam, S. Ghosh, R. K. Biswas, A. Saxena, A. Raja, M. O. Thotiyl, S. Wadhai, A. G. Banpurkar, and J. Kundu, "Solution chemistry-based nanostructuring of copper dendrites for efficient use in catalysis and superhydrophobic surfaces." *RSC Adv.*, **6**, 8416 (2016).
34. R. C. Brower, D. A. Kessler, J. Koplik, and H. Levine, "Geometrical approach to moving-interface dynamics." *Phys. Rev. Lett.*, **51**, 1111 (1983).
35. O. Zik and E. Moses, "Electrodeposition: the role of concentration in the phase diagram and the Hecker transition." *Phys. Rev. E*, **53**, 1760 (1996).
36. E. Ben-Jacob and P. Garik, "The formation of patterns in non-equilibrium growth." *Nature*, **343**, 523 (1990).
37. B. Utter and E. Bodenschatz, "Dynamics of low anisotropy morphologies in directional solidification." *Phys. Rev. E*, **66**, 051604 (2002).
38. K. Ankit and M. E. Glicksman, "Growth competition during columnar solidification of seaweed microstructures: Insights from 3-D phase-field simulations." *Eur. Phys. J. E*, **43**, 14 (2020).
39. P. P. Trigueros, F. Sagués, and J. Claret, "Influence of an inert electrolyte on the morphology of quasi-two-dimensional electrodeposits." *Phys. Rev. E*, **49**, 4328 (1994).
40. L. Lopez-Tomas, J. Mach, P. P. Trigueros, F. Mas, J. Claret, and F. Sagues, "Quasi-twodimensional electrodeposition: A summarized review on morphology and growth mechanisms." *Chaos, Solitons Fractals*, **6**, 287 (1995).
41. F. Battal, N. Gupta, R. Pranger, J. Maasen, P. Mulder, R. Poelma, E. Vlieg, and J. Schermer, "Organics-free porous nano-dendritic cu films for high-power packaging interconnects." *IEEE 76th Electronic Components and Technology Conference (ECTC)* (2026), (Submitted).